Size-dependent melting point depression of nanostructures: Nanocalorimetric measurements

M. Zhang, M. Yu. Efremov, F. Schiettekatte, E. A. Olson, A. T. Kwan, S. L. Lai, T. Wisleder,
J. E. Greene, and L. H. Allen*

*Material Science and Engineering and Coordinated Science Laboratory, University of Illinois at Urbana-Champaign,
Urbana, Illinois 61801*

The melting behavior of 0.1–10-nm-thick discontinuous indium films formed by evaporation on amorphous silicon nitride is investigated by an ultrasensitive thin-film scanning calorimetry technique. The films consist of ensembles of nanostructures for which the size dependence of the melting temperature and latent heat of fusion are determined. The relationship between the nanostructure radius and the corresponding melting point and latent heat is deduced solely from experimental results (i.e., with no assumed model) by comparing the calorimetric measurements to the particle size distributions obtained by transmission electron microscopy. It is shown that the melting point of the investigated indium nanostructures decreases as much as 110 K for particles with a radius of 2 nm. The experimental results are discussed in terms of existing melting point depression models. Excellent agreement with the homogeneous melting model is observed.

I. INTRODUCTION

The physical properties of materials with reduced dimensions draw considerable attention because of the technological importance and fundamental interest of the problem.[1,2] Nowhere is the interest greater in the thermodynamics of materials at small dimensions than in the microelectronics industry, where transistors and metal interconnects will have tolerances of only several nanometers by the year 2005. One particular phenomenon of interest is the size-dependent melting point depression—small particles have a lower melting point than bulk material.[3–5] This results from the increasingly important role of the surface as the size of the structures decreases. From an atomistic point of view, as the size of the nanostructures decreases an increased proportion of atoms occupy surface or interfacial sites. These atoms are more loosely bound than bulk atoms, which facilitates the melting of the nanostructure. However, the mechanism by which nanostructures melt is not fully understood. In order to develop a better understanding of the phenomenon more experimental information is warranted, especially with regard to the energy associated with the melting process.

Melting point depression in nanostructures was first observed using transmission electron microscopy (TEM).[3,6–8] Using this technique the melting temperature of nanostructures is monitored by the loss of crystalline structure with increasing temperature. It can also be used, as we do in this work, to measure the size of the nanostructures directly. However, high-energy beam-sample interactions may influence the melting process. Similarly, x-ray diffraction has also been used for melting point depression studies.[9,10] The difficulty in using this method is the determination of the particle size distribution, especially for the smaller particles.

Calorimetry is another extremely powerful technique for investigations of melting phenomenon. Using calorimetry we directly measure the heat capacity and the latent heat of fusion as functions of the temperature. This technique has undergone major improvements in recent years. Calorimetry adds a unique dimension to melting point studies. In addition to obtaining melting point information we also obtain values for the energy involved in the melting process. There are many types of calorimetric methods. Experiments with metal filled porous substances,[11] particles dispersed in oil,[12] and particles embedded in a metal matrix[13,14] used conventional calorimetry, but the melting behavior in such cases must strongly depend on the type of surrounding material, i.e., on the environment of the nanostructures.[14,15] Also, a sophisticated technique based on laser irradiation of free metal clusters produces calorimetric data which are not affected by substrate influence.[16,17] To date, this technique has been applied only for very small single clusters (compatible with mass spectrometry).[16]

Recently, an ultrasensitive method, thin-film differential scanning calorimetry (TDSC),[18–21] was developed to measure the thermal processes occurring in samples deposited on a surface. In this article, the TDSC method is used to observe the melting behavior of small indium nanostructure ensembles (indium and its alloys are important materials in the microelectronics area, specifically in flip-chip packaging technology[22]). The limits of the measurement have been pushed to sizes never before reached. We demonstrate that the melting point depression and latent heat of fusion of such nanostructures decreases proportionally to the reciprocal radius r^{-1} for radii down to 2 nm.

II. MELTING MODELS

There are many excellent approaches for theoretical studies of melting phenomenon in small particles, including classical thermodynamic as well as modern simulation methods.[5,23] For convenience in describing our experimental work, in this paper we will use the classical thermodynamic description of melting. A theory based on the Laplace equation of the surface and the Gibbs-Duhem equation[24] predicts a melting temperature depression of the form[9]

$$\Delta T = T_m^{\text{bulk}} - T_m(r) \approx \frac{2 T_m^{\text{bulk}}}{H_m^{\text{bulk}} \rho_s} \frac{\alpha}{r}, \qquad (1)$$

where T_m^{bulk}, H_m^{bulk}, and ρ_s are the bulk melting temperature, the bulk latent heat of fusion, and the solid phase density, respectively. r represents the radius of a spherical particle, and α is a parameter related to the interfacial tension between the solid phase and its environment. Up to now, three main melting mechanisms have been considered to describe the relation between the melting temperature and the size of particles, resulting in different expressions for α.

(i) The homogeneous melting and growth model (HGM),[6,25] which considers equilibrium between entirely solid and entirely melted particles and expresses α as

$$\alpha_{\text{HGM}} = \sigma_{sv} - \sigma_{lv}(\rho_s/\rho_l)^{2/3}. \tag{2}$$

(ii) The liquid shell model (LSM),[6,26,27] which differs from the HGM by assuming the presence of a liquid layer of thickness r_0 in equilibrium at the surface of solid particle; this model sets

$$\alpha_{\text{LSM}} = \frac{\sigma_{sl}}{1 - \dfrac{r_0}{r}} + \sigma_{lv}\left(1 - \frac{\rho_s}{\rho_l}\right). \tag{3}$$

(iii) The liquid nucleation and growth model (LNG),[28–31] based on the kinetic consideration that melting starts by the nucleation of liquid layer at the surface and moves into the solid as a slow process with definite activation energy, and for which

$$\sigma_{sl} < \alpha_{\text{LNG}} < \frac{3}{2}\left(\sigma_{sv} - \sigma_{lv}\frac{\rho_s}{\rho_l}\right). \tag{4}$$

Here σ represents the interfacial tension between solid, liquid, and vapor phases (indexes s, l, and v, respectively), and ρ_l is the density of the liquid phase. In addition, it is worth mentioning that Eq. (1) is actually a first-order expansion. However, the second-order term[32] is small in the present case, since it represents a correction of $+5$ K at $r = 2$ nm.

These models are related to the different proposed melting mechanisms of the nanostructures. Verifying the applicability of these models by the experimental data (without presupposing any model in the data analysis) allows us to draw conclusions about the melting mechanism of indium particles.

III. EXPERIMENT

The TDSC method relies on microfabricated calorimetric sensors. The planar and cross-sectional configurations of the TDSC system are shown in Fig. 1. These sensors consist of an extremely thin (30 nm) amorphous silicon nitride membrane (a-SiN$_x$) supported by a silicon frame. The mass addenda of the sensor being so small, the achieved sensitivity is comparable to the latent heat of fusion of 1/1000 of a monolayer of bulk indium.

On one side of the membrane, a patterned thin (50 nm) nickel strip is deposited, which is used simultaneously as a heater and resistive thermometer during the experiments. Differential calorimetry is achieved by using two identical sensors in one setup—a sample sensor (with material deposited on the sensor) and a reference sensor (with no material). Before the experiment, the resistivity of both sensors is cali-
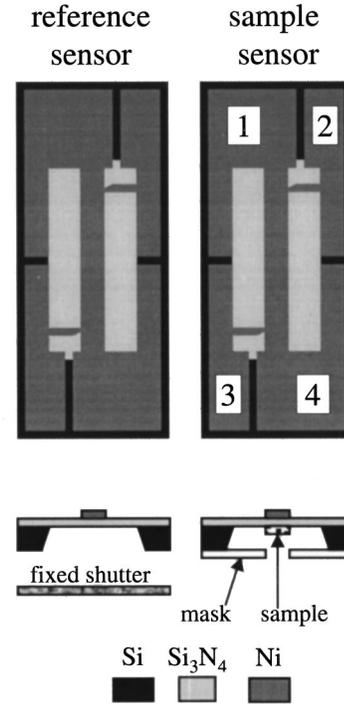

FIG. 1. Plan-view and cross-sectional representations of the thin-film calorimeters used for this study. The current pulse is driven between paddles 1 and 4, and the voltage is measured across the central part of the calorimeter using paddles 2 and 3. Differential measurements are achieved by using a second calorimeter on which no sample is deposited.

brated against the temperature in a three-zone tube vacuum furnace.

The calorimetric measurement is initiated by applying a synchronized dc electrical pulse to each nickel heater. The temperature of the sensors increases by Joule heating. High heating rates (from 10^4 to 10^6 K/s) allow the measurements to approach adiabatic conditions. The current and voltage of the sensors are measured for power and resistivity (and temperature) calculations.

In the ideal case where we would have two identical sensors with temperatures increasing exactly at the same rate, the power required to melt the sample deposited on the sample calorimeter would simply be

$$P(t) = V_S I_S - V_R I_R, \tag{5}$$

where V and I denote the voltages and currents through the sample and reference (indexes S and R, respectively) sensors, and t is time. The heat capacity would then be

$$C_P(T) = \frac{P(t)}{dT/dt}, \tag{6}$$

where T is the sample temperature at time t. However, several corrections have to be taken into account. First, an independent measurement of V and I for the sample and reference leads to somewhat noisy measurements. A differential measurement of the voltage across the reference and sample sensors drastically improves the signal-to-noise ratio, and is the key element that allows us to reach high sensitivity. Second, the characteristics of the sensors in any couple are not

absolutely identical. In order to correct this disparity, the difference in heat capacity between the sample and reference cells is measured as a function of temperature before the experiments. Such relations are used in the final calculations. Corrections also take into account the influence of the deposited sample mass on the heating rate of the sample sensor. Third, the same $C_P(T)$ measurements are carried out at different heating rates, and used for later calculations of heat loss correction (i.e., departure from adiabatic conditions).

For the present experiments, thin indium layers with different thicknesses have been investigated. We selected indium due to its low melting point ($T_m^{bulk} = 156.60\,°C$)[33] and low affinity with SiN_x. Moreover, indium has frequently been used for investigations of melting phenomena in small particles.[6,7,11,13,14,30,34] The first stages of the deposition result in a discontinuous film on the sensor membrane, consisting of nanoparticles of various sizes.[35] Below 100 nm of equivalent indium thickness, the average size of the particles increases almost linearly with the quantity of metal deposited.

For each experiment, both sensors are placed together in a standard evaporator with a base pressure of about 10^{-8} Torr. Before the deposition, the sensors are heated in order to remove any potential contamination of the surface. A shadow mask is placed in line with the nickel strip as illustrated in Fig. 1. Pure indium (Alfa Æesar 99.9985%) is then evaporated onto the sample sensor to nominal thicknesses ranging from 0.1 to 10 nm. The thickness of the different layers is monitored by an *in situ* quartz microbalance, and corroborated afterward by the mass obtained from the heat capacity measurements. The deposition rate ranged from 0.02 to 0.04 nm/s.

Beginning within a few seconds following the indium deposition, 100 calorimeter measurements/scans are taken sequentially at 1-s intervals. During each scan the temperature of the nanostructures as well as the calorimeter is raised from ambient temperatures to 300 °C. Consequently the nanostructures are annealed during each scan. However, the effects of annealing, which are associated with minor changes in the particle size distribution (TEM) and C_p data, are limited mostly to the first scan and will be the focus of our future work. The calorimetry data presented in this paper represents the average of all 100 scans excluding the first ten scans. The scans are identical within the measurement error, and are averaged in order to increase the sensitivity of the system. The TEM and calorimetry data presented here represent the results of fully annealed indium particles.

After the calorimetric measurement, the sample sensor is transferred *ex situ* into a Phillips CM-12 TEM without additional preparation. Bright-field micrographs of the sample sensor are taken. The particle-size distributions corresponding to each calorimetric experiment are obtained from digitized images using a combination of distance transformation and blob analysis algorithms.[36] Several thousand particles were measured in each sample in order to achieve sufficient statistics.

Oxidation of indium nanostructures occurs during the transfer of sample from the deposition/calorimetry chamber to the TEM system. Particles with a radius of less than 3 nm are completely oxidized while those nanostructures with a radius larger than 3 nm have an ''oxide-shell'' of 3-nm
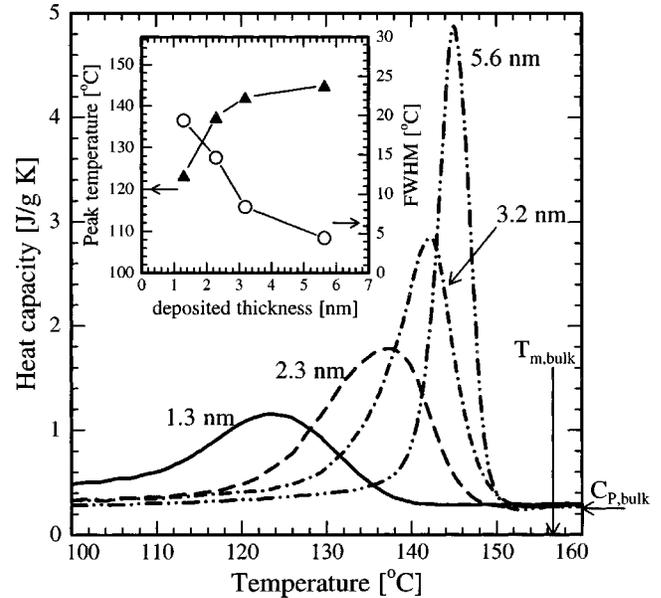

FIG. 2. Normalized calorimetric curves [i.e., $C_P(T)/mass$] obtained for the 1.3-, 2.3-, 3.2-, and 5.6-nm indium depositions. The inset shows the progression of the peak temperature and the full width at half maximum (FWHM) of the melting peak with deposited thickness.

thickness.[34] We correct for the increase in particle size due to oxidation by recalculating the particle-size distribution obtained from the TEM micrographs. By taking into account the change in volume (24% in volume or 7% change in radius) due to the oxidation process we reduce the size of each particle in the distribution by the appropriate amount. For example an indium nanoparticle with radius of 3.0 nm will be totally oxidized during the transfer, and will have a final radius of 3.2 nm. From a practical standpoint, the oxidation effect has little impact on the overall analysis, since the maximum difference between the radius of an completely oxidized and unoxidized 3.0-nm particle is only 0.2 nm, which is about the level of uncertainty of our TEM and image analysis techniques.

We note that particle smaller than ~1 nm were not distinguishable from the small features in the SiN_x membrane. However, such small particles should not contribute significantly to the melting heat unless they are present in huge proportions. Finally, the relation between the melting point and the particle size is extracted from the correspondence between the calorimetric data and the particle size distributions, as described in Sec. IV B.

IV. RESULTS AND DISCUSSION

A. Effects of the melting point depression on TDSC measurements

Figure 2 shows the heat capacity $[C_P(T)]$ measurement for indium films with thickness ranging from 1.3 to 5.6 nm. These curves have been normalized, i.e., divided by the film area S and the amount of mass deposited, from 0.4 ng (1.3 nm) to 1.7 ng (5.6 nm). The baseline of all the curves corresponds to the heat capacity of bulk indium at higher temperatures. This corroborates well with the amount of indium measured by the quartz microbalance during the deposition.
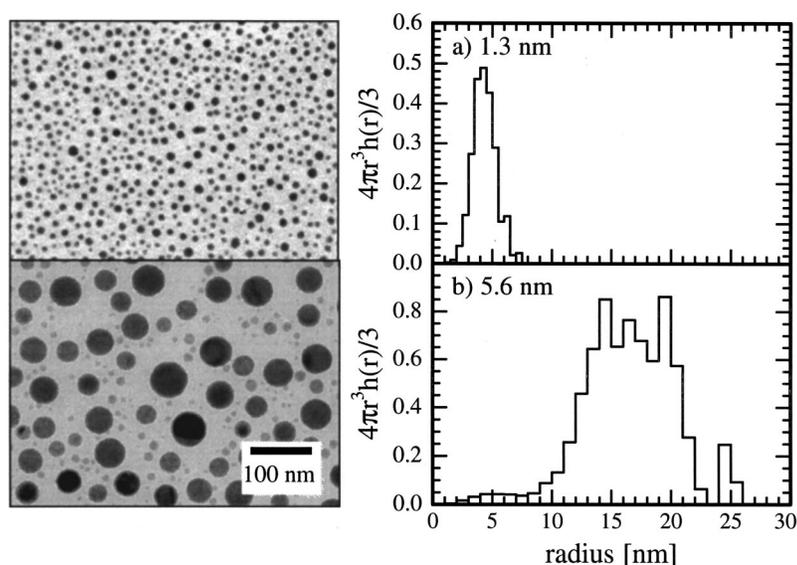
FIG. 3. Micrographs and associated particle size distribution of the (a) thinnest and (b) thickest samples of Fig. 2. The particle size distributions (in [particles/nm^2]/nm) are multiplied by the volume of the particles ($4\pi r^3/3$), so the vertical axis have no dimensions.

As a result, this shows that the calorimeter can be used to measure small masses of material precisely.

The peak in each $C_P(T)$ measurement represents the heat involved in the melting process as a function of the temperature. Figure 2 demonstrates a significant low-temperature shift in melting peak and peak broadening as the film thickness decreases. These effects are reported on the inset of Fig. 2, which shows the position of the peaks and their full width at half maximum (FWHM) as a function of the indium film thickness. This is the result of the decreasing size of the particles with decreasing deposited amount of indium.

The TEM micrographs in Fig. 3 show that the indium film is discontinuous and consists of individual nanometer-size particles. The smaller particles correspond with the thinner film, as clearly shown by the corresponding particle-size distributions. The particle distribution histograms, hereafter denoted as $h(r)$, represent the particle surface density as a function of the radius [i.e., (particles/nm^2)/nm]. In Fig. 3 and subsequent figures, $h(r)$ has been multiplied by the volume of the particles ($4\pi r^3/3$) so it reflects in a more sensible way the participation of the particles to the melting peak, since they should contribute to the heat of melting proportionally to their volume, or mass, at least in a first approximation.

On these histograms it is shown that average size of particles decreases with the film thickness. Since their temperature of melting decreases accordingly, following Eq. (1), their contribution to the melting peak is shifted toward lower temperature. The broadening of the peak is the result of the nonlinear ($1/r$) relation between the size of the nanostructures and their melting point. The same spread in the particle size distribution corresponds to a much larger width in the $C_P(T)$ curve for smaller particles than for larger ones. It is thus clear that a relation between the size of the nanostructures and their melting temperature can be extracted from such measurements.

Another important feature of calorimetric techniques is that they simultaneously measure the latent heat of fusion of the melting particles. This is important since the size can also influence this parameter. The proportion of atoms occupying surface sites in a spherical particle will increase proportionally to the reciprocal radius ($1/r$), at least in a first approxi-

mation. Such atoms being more loosely bounded, they should require less heat in order to melt, so we also expect the latent heat of fusion to decrease with particle size.

The value of the heat of fusion H_m can be determined from the $C_P(T)$ curves as the area under the melting peak. The melting peak component of the $C_P(T)$ measurements shown in Fig. 2, as well as those of other experiments, have been integrated over the temperature in order to measure the heat of melting as a function of film thickness. This result is shown in Fig. 4, in comparison to the expected value if all particles were melting with the bulk latent heat of melting (solid line). While the correspondence is very good for larger thicknesses, it is seen that the heat of melting is significantly offset for the smaller particles. This difference can be due in
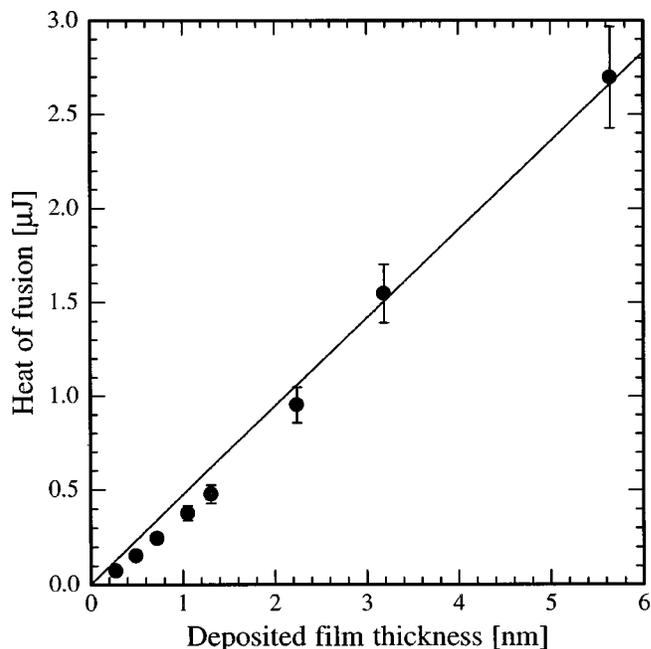

FIG. 4. Raw data of the heat of fusion (integral of the melting peak) as a function of the deposited thickness for all the experiments. The solid line represents the expected value if all the deposited indium melted with the bulk heat of fusion.
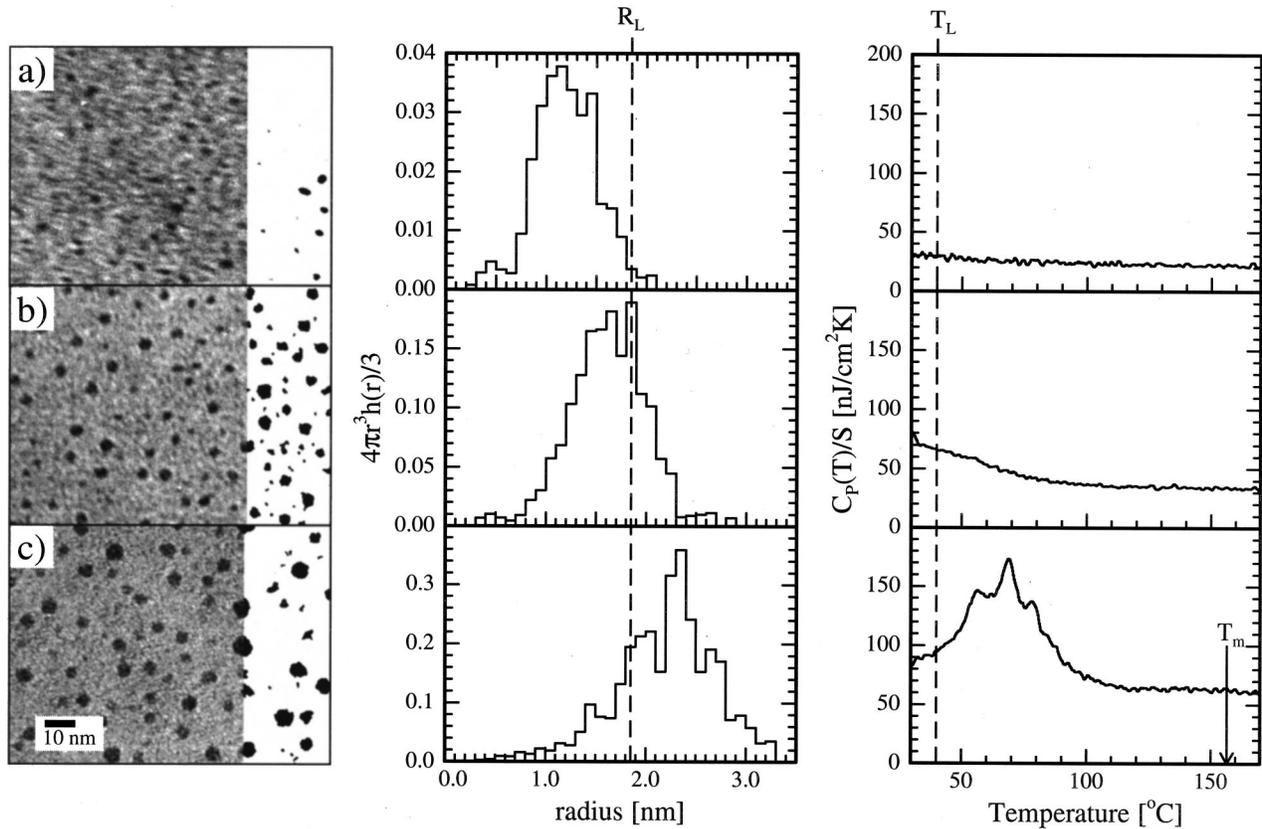
FIG. 5. Micrographs, particle size distribution and associated calorimetric data for the (a) 0.1-, (b) 0.2-, and (c) 0.4-nm indium depositions. The radius R_L corresponding to the lower limit temperature T_L is indicated.

part to a size-related depression of the latent heat, but also to possible existence of some forms of deposited indium which do not contribute to the melting process under the described experimental conditions. Such forms can include already melted particles, adatoms, the liquid layer on the surface of particles, the interface layer between particles and membrane, etc.

B. Size-dependent effects

This section describes how the influence of the size on the melting point and heat are determined for indium nanostructures. The interconnection between the $C_P(T)$ plots, obtained from calorimetry, and the particle-size distribution $h(r)$, observed by microscopy, is based on the fact that particles with different sizes melt differently. The relationship between those two measurements is based on (i) the particle size dependence of the melting temperature and (ii) the relation between the size and the latent heat of fusion. These two phenomena are tightly intertwined in the measured signals. Our objective here is to decouple and reveal these two effects without using any *a priori* insight or model for their size dependence.

Only two general assumptions will be used. First, the melting temperature increases with size (i.e., particles with larger radius melt at higher temperatures). Second, each particle melts instantly (at one certain temperature). These suppositions are very common. The first hypothesis is based on
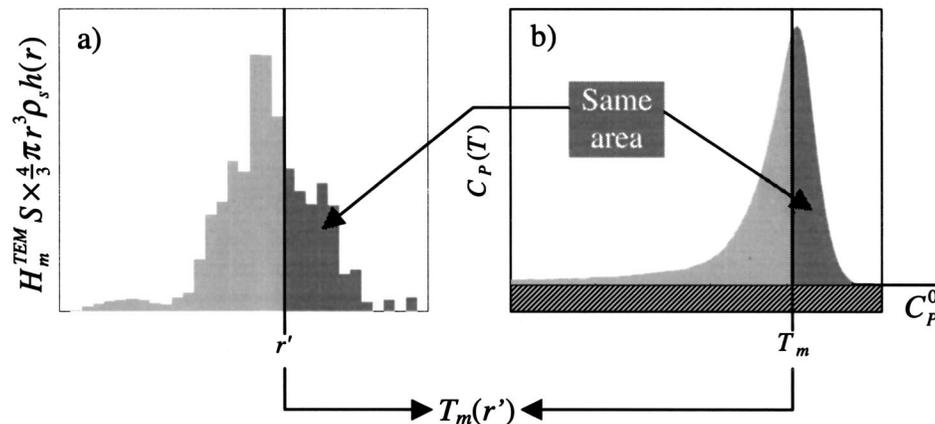

FIG. 6. Schematic representation of the procedure used to determine the relationship between the melting temperature T_m and the particles radius r. (a) The normalized particle size distribution, which has the same area under the curve than the melting peak in (b) which is the corresponding calorimetric curve. The temperature T_m at which the particles with a radius r melt is such that the area under the right part of both curves is equal.

extensive experimental literature on the melting of small particles on free surfaces. The only exception is for very small clusters,[16,17] which show irregular variations of the melting point. The second assumption is used explicitly in HGM (Ref. 6) and LSM (Ref. 6) models, and obtained as experimental fact in LNG model considerations.[30]

1. Size dependence of the melting point

The main idea of extraction of a model-free correspondence between melting temperature and particle radius from TEM and calorimetric data is straightforward. A direct relationship is established by mapping (i.e., integrating concurrently) the area under the particle-size distributions and the melting peak of the corresponding $C_P(T)$ measurements. This integration procedure will be described below. However, before we enter into the details of this calculation, it must be established that both the size distribution histograms and melting peak plots are incomplete in the lower part of their abscissa. While the maximum melting temperature, near T_m^{bulk}, is properly measured, as well as the largest particle sizes in each film, particles with a radius less than about 1 nm cannot be distinguished from the SiN$_x$ membrane features on TEM micrographs. So this part of the histogram has the largest degree of uncertainty. At the same time, a part of the melting peak, for temperatures below the present working temperature range of calorimeter, cannot be measured. This will obviously principally affect the thinnest films.

In order to find the section of the size distribution that corresponds to the measured part of the melting peak, we need to calculate a particle radius R_L that corresponds to our lowest measurable melting temperature T_L. Then the particle distribution from R_L up to its maximal radius (which is easily found from the TEM micrographs) can be mapped onto the melting peak in the temperature range from T_L up to its maximal temperature. The following procedure has been used to calculate the value of R_L. Although the working temperature range of our TDSC begins at room temperature, reliable $C_P(T)$ measurements are available only above 40 °C due to transient effects at the beginning of the heating pulse. It is thus convenient to use this temperature as T_L (i.e., $T_L = 40$ °C).

The $C_P(T)$ curves and the particle radius distributions of the smallest deposited thicknesses are compared in Fig. 5. For the 0.4-nm indium deposition, most of the melting peak is visible, and a large fraction of the indium mass is contained in the particles larger than 2 nm in radius. Also, the 0.2-nm experiment reveals barely half of the melting peak in the $C_P(T)$ data. On the other hand, there is no observable melting peak in the 0.1-nm $C_P(T)$ measurement, for which all particles are smaller than 1.75 nm in radius. After comparing the particle distribution with the heat-capacity data for the thinnest films (0.1–0.4 nm) we conclude that the most reasonable estimation of $R_L = 1.85 \pm 0.1$ nm. Henceforth for all further analysis, only particles with radius larger than R_L will be considered to contribute to the melting heat above T_L.

This being established, the next step is to relate the specific melting point $T_m(r)$ to a specific particle size. This is achieved by *mapping* the integral heat involved during the melting [from the $C_P(T)$ measurements] with the corresponding TEM particle distribution $h(r)$ (for $r > R_L$) for
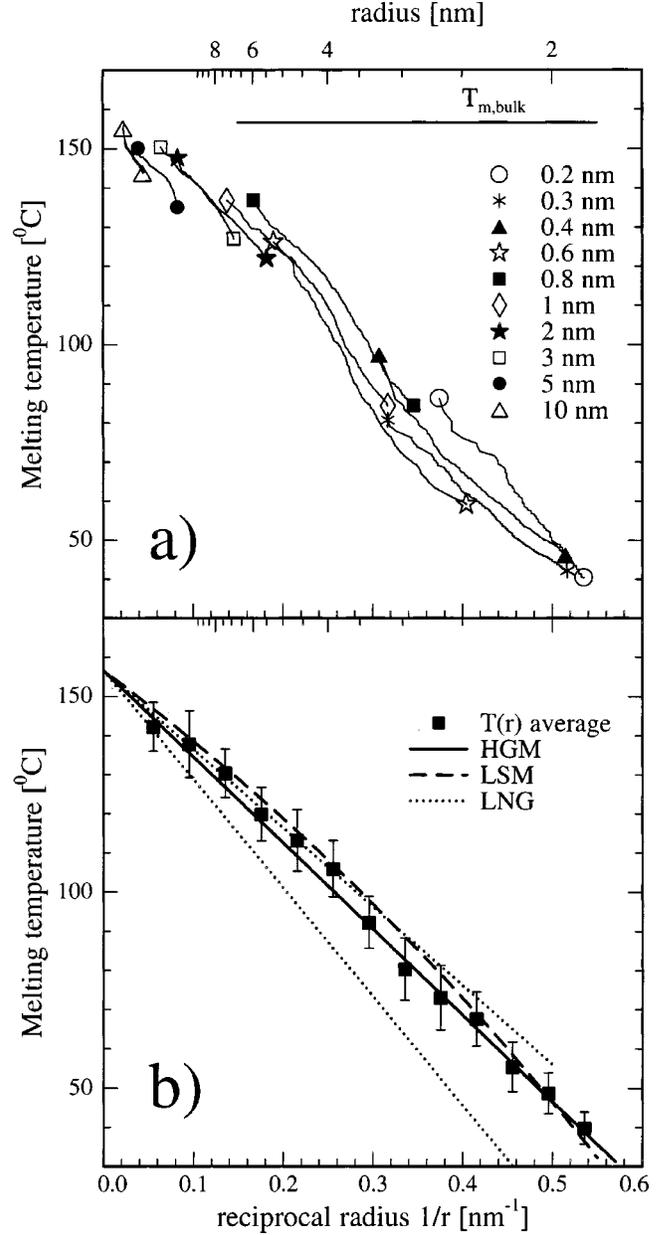

FIG. 7. Result of the calculation schematically described in Fig. 6 as a function the reciprocal radius. (a) Result for each experiment, for which both ends are identified by the same symbol. (b) Average of the results in (a) (symbol ■). This average result is compared with different melting models (lines).

each deposition cycle. This mapping process is shown schematically in Fig. 6.

The first step is to "normalize" the calorimetry and TEM data so that the heat generated by a specific set of particles is equal to the heat measured by the calorimeter. In doing so we define the average heat of fusion H_m^{TEM} for the specific deposited thickness to be as follows:

$$H_m^{TEM} = \frac{\int_{T_L}^{T_m} [C_P(T) - C_P^0] dT}{S \int_{R_L}^{\infty} \frac{4}{3} \pi r^3 \rho_s h(r) dr}, \qquad (7)$$

TABLE I. Characteristics of indium.

Constant	Value	Description	Ref.
T_m^{bulk}	429.75 K	bulk melting point	33
H_m^{bulk}	28.39 J/g	bulk specific heat of fusion	33
ρ_s	7.31 g/cm^3	solid phase density	34
ρ_l	7.02 g/cm^3	liquid phase density	33
σ_{sv}	618 ± 10 mJ/m^2	solid-vapor interfacial tension[a]	37
σ_{lv}	560 mJ/m^2	liquid-vapor interfacial tension	37
σ_{sl}	63 mJ/m^2	solid-liquid interfacial tension	37,9
c_P	$(0.211\,856 + 9.1160 \times 10^{-5}\,T)$ J/g K, $T < T_m$		
	0.27348 J/g K, $T > T_m$	specific heat capacity	38

[a]Average between (110) and (011) faces.

where C_P^0 is the baseline under the melting peak in the $C_P(T)$ measurement, and corresponds to the bulk heat capacity, ρ_s is the bulk solid phase specific density, and S is the area of the indium film. Although it is necessary for us to define the heat of fusion in this way to directly relate the particle size and melting point, another method to estimate the dependency of the heat of fusion H_m on particle size will be discussed in Sec. IV B 2.

The calculation of the mapping proceeds as follows. In order to determine the melting temperature $T_m(r)$ for a particle of radius r, we integrate the equivalent heat of melting for all particles with radius $r > r'$ [the shaded area under the curve in Fig. 6(a)] as given by the integral

$$H_m^{\text{TEM}} \times S \int_{r'}^{\infty} \frac{4}{3} \pi r^3 \rho_s h(r) dr. \qquad (8)$$

We then match this amount of heat with that measured with the calorimeter (the shaded area under the curve in Fig. 6(b) as given by Eq. (8). This is done by selecting the appropriate value for the lower limit of the following integral:

$$\int_{T_m(r')}^{T_m^{\text{bulk}}} [C_P(T) - C_P^0] dT. \qquad (9)$$

For a given value of r' there is a unique value of $T_m(r')$ which satisfies the criterion. Obviously, because of the definition of H_m^{TEM} [Eq. (7)], at $r' = R_L$ we find $T_m(r) = T_L$. This technique is repeated sequentially for the entire range of particles size starting from the largest particle to the minimum size particle with the constraint that $r' > R_L$.

The mapping process is done separately for each deposited thickness, each yielding a unique experimental set of values for $T_m(r)$. The results of this analysis are shown in Fig. 7(a). The beginning and end of the relation deduced for each thickness are identified by the same symbol. Several

TABLE II. Experimental parameters.

Parameter	Value	Description
S	2.3 mm^2	area of the indium film
T_L	40 °C	lower-limit temperature
R_L	1.85 ± 0.1 nm	lower limit radius
Q	0.75 ± 0.1	volume shape factor
r_0	<0.5 nm	liquid shell thickness in LSM

depositions have been performed with various amounts of material. Since there is some overlap in the particle distributions between the deposited thicknesses, we can obtain an average value for $T_m(r)$. Such average $T_m(r)$ relations are calculated, and plotted in Fig. 7(b), and are found to be remarkably linear over a wide range down to nanometer sizes.

Such "classical" behavior is predicted by the HGM model. To illustrate this point, a simple straight-line relation, identified as a thick solid line in Fig. 7(b), has been fitted to the averaged data. The slope of this relation is -220 ± 10 nm K, which corresponds to $\alpha = 53 \pm 3$ mJ/m^2 in Eq. (1). A theoretical value of α can be calculated for the HGM from Eq. (2) using values denoted in Table 1. The result, $\alpha_{\text{HGM}} = 43 \pm 10$ mJ/m^2, is in fairly good agreement with the experimental value (also see Table II).
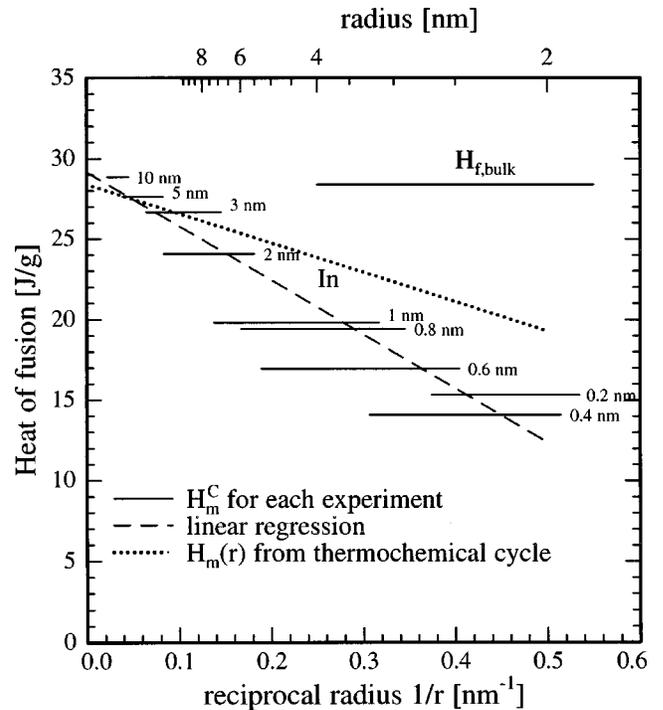

FIG. 8. Heat of fusion as a function of the reciprocal radius deduced from the melting peak and the estimated melting mass of each experiment (see Sec. IV B 2 for the details of the calculation). The horizontal solid lines indicate the radius range to which the calculation applies in each case. The dashed line is a linear regression through the data. The doted line represents the theoretical size-dependence deduced from the thermochemical cycle of Fig. 9.
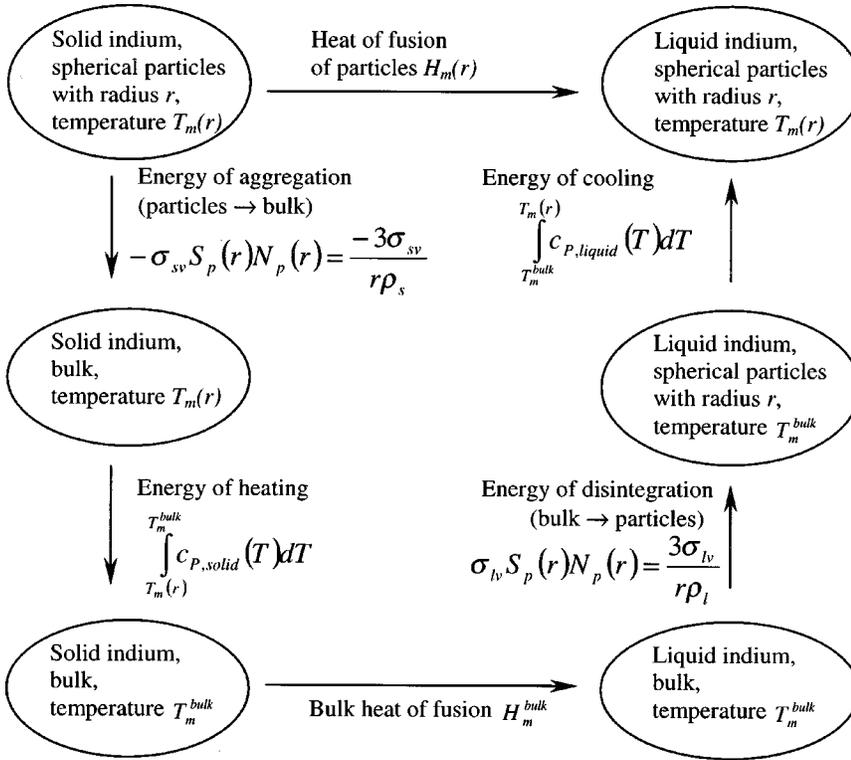
FIG. 9. The thermochemical cycle, used to estimate the size dependence of the latent heat of fusion $H_m(r)$ using Hess' Law. $S_p(r)$ and $N_p(r)$ denote the area of particles and the number of particles that can be made from 1 g of indium, respectively; see the text for other definitions.

Our results do not exclude the LSM model, but impose a serious limit on the thickness of the liquid shell r_0. The dashed line in Fig. 7(b) represents a fit of the LSM to the unaveraged data, giving $r_0 = 0.3$ nm and $\sigma_{sl} = 63$ mJ/m^2 $\approx \sigma_{sv} - \sigma_{lv}$ as it should be near the melting temperature.[9] The maximum acceptable value for $r_0 = 0.5$ nm, which represents the thickness of two atomic monolayers. This maximum value for r_0 is obtained by allowing r_0 to vary, yet keeping the fitted curve within bounds of the errors bars of the data. This is in interesting agreement with the results of Ref. 37 on bulk (110) indium; these authors observed a strong relaxation effect in the two first monolayers of this material. Our data also fall in the limit range predicted by the LNG model. Nevertheless, no physical evidence allows us to determine if the additional parameters in the LSM (r_0) and LNG models are physically meaningful. For this reason, the simplest HGM model, which can be described in terms of some well-known independent characteristics of the material (σ_{sv}, σ_{lv}, ρ_s, and ρ_l), is preferred.

Finally, the slight S shape denoted in some of the individual $T(r)$ relations in Fig. 7(a) could be the result of the widening of the melting peaks by the temperature resolution function of the calorimeters (the FWHM is approximately equal to 4 K); but some real effects could also be responsible for such features.

2. Size dependence of the latent heat of fusion

Now that the relation between the melting temperature and the size of the particles has been extracted from the C_P measurements, the next step is to look at the relation between the heat of fusion and the radius. The specific heat of fusion H_m is calculated by dividing the heat involved in the melting process by the mass of the sample. In one case, the mass of the sample can be evaluated from the volume of the particles measured from the TEM micrograph. This type of calculation leads to the value H_m^{TEM} used in Sec. IV B 1.

However, such a volume estimate is influenced by several parameters, mainly the shape of the particle. TEM only allows a two-dimensional projection measurement of the particles, which may not be complete spheres. In fact, a noticeable departure of about 25% is found between the volume measured by TEM and the expected deposited thickness. For indium films in the range of 0.2–5 nm, particles can be viewed as incomplete spheres with a volume shape factor $Q = 0.75 \pm 0.1$ (i.e., the actual volume of the particles is about 75% of the what it would be if they were complete spheres with the radius measured by TEM).

On the other hand, the mass can be deduced directly from the baseline in the $C_P(T)$ measurement, using the bulk specific heat capacity. In this case, a self-consistent estimate of the specific heat of fusion can be found,

$$H_m^C = \frac{\int_{T_L}^{T_m^{\text{bulk}}} [C_P(T) - C_P^0] dT}{C_P^0/c_P F}, \qquad (10)$$

where F is a correction factor discussed below, and C_P^0/c_P is the mass found from the ratio between the measured baseline heat capacity (C_P^0 in J/K) and the specific-heat capacity from the literature (c_P in J/g K).[38] However, this ratio constitutes a measurement of the total mass. As demonstrated in Sec. IV B 1, the melting peak is incomplete for many experiments, especially for the smaller thicknesses, since the particles smaller than R_L do not contribute to the melting above T_L. For a better approximation, only the fraction F of the total mass actually melting has to be taken into account. F

can be estimated using the histograms $h(r)$ as the volume fraction of particles with a radius above R_L over the total volume measured by TEM.

However, inasmuch as TEM has a limited resolution, and could not detect a large number of very small particles, only an upper-limit estimation of F is available. Thus H_m^C constitutes a lower-limit estimation of the specific heat of fusion.

The results of the calculation of Eq. (10) for each experiment are presented in Fig. 8. The horizontal lines represent the radius range to which this calculation applies, considering the spread of the particles distribution in each case. While the H_m^C value tends very well to the bulk latent heat of fusion for large particles ($1/r \to 0$), it clearly shows a depression as the particle size decreases.

While we have to keep in mind that this calculation constitutes a lower estimate, from an atomistic point of view this depression corresponds to the heat necessary to melt approximately the first two atomic monolayers of the particles. In some sense, this would indicate that the atoms of the first outer two monolayers of the indium particles are in a relaxed, liquidlike state, and do not contribute to the melting process. This conclusion is similar to that deduced from the maximum acceptable value of r_0 in the LSM discussed in Sec. IV B 1.

The latent heat of fusion is expected to be size dependent from theoretical considerations.[11] A more rigorous treatment using Hess' law,[39] and illustrated by the thermochemical cycle of Fig. 9, allows us to estimate the latent heat of fusion depression from a classical thermodynamics point of view:

$$H_m(r) = H_m^{\text{bulk}} - \frac{3}{r}\left(\frac{\sigma_{sv}}{\rho_s} - \frac{\sigma_{lv}}{\rho_l}\right)$$

$$- \int_{T_m(r)}^{T_m^{\text{bulk}}} [C_{P,\text{liquid}}(T) - c_{P,\text{solid}}(T)] dT. \quad (11)$$

The size-dependent heat of fusion $H_m(r)$ is represented as a dotted line in Fig. 8. The model is in fairly good agreement with our data. The difference can be justified in terms of an underestimate of both H_m^C [Eq. (10)] and σ_{sv} [in Eq. (11)].

V. CONCLUSION

Using ultrasensitive thin-film differential scanning calorimetry in combination with *ex situ* TEM analysis, the melting point depression of indium nanostructures has been deduced quantitatively down to particle radii of 2 nm. A model-free method of calculating the melting temperature— the particle radius relation—was described. The melting point shows a linear decrease with curvature ($1/r$) within the experimental uncertainty, which is compatible with the homogeneous melting mechanism. It was also shown that the theoretical considerations of latent heat of fusion depression with increasing curvature are in reasonable agreement with our experimental results.

*Email address: L-ALLEN9@uiuc.edu

[1] *Nanoparticles and Nanostructured Films: Preparation, Characterization and Applications*, edited by J. H. Fendler (Wiley-VCH, Weinheim, 1998).

[2] K. N. Tu, J. W. Mayer, and L. C. Feldman, *Electronic Thin Film Science for Electrical Engineers and Materials Scientists* (Macmillan, New York, 1992).

[3] M. Takagi, J. Phys. Soc. Jpn. **9**, 359 (1954).

[4] R. S. Berry, Sci. Am. (August), 68 (1990).

[5] G. Bertsch, Science **277**, 1619 (1997).

[6] P. A. Buffat and J. P. Borel, Phys. Rev. A **13**, 2287 (1976).

[7] C. J. Coombes, J. Phys. F: Met. Phys. **2**, 441 (1972).

[8] G. L. Allen, R. A. Bayles, W. W. Gile, and W. A. Jesser, Thin Solid Films **144**, 297 (1986).

[9] K. F. Peters, J. B. Cohen, and Y.-W. Chung, Phys. Rev. B **57**, 13 430 (1998).

[10] P. M. Ajayan and L. D. Marks, Phys. Rev. Lett. **63**, 279 (1989).

[11] K. M. Unruh, T. E. Huber, and C. A. Huber, Phys. Rev. B **48**, 9021 (1993).

[12] G. T. Fei, K. Zheng, Z. Q. Chu, Y. Qin, L. D. Zhang, and L. Liu, Mater. Res. Bull. **32**, 857 (1997).

[13] H. Saka, Y. Nishikawa, and T. Imura, Philos. Mag. A **57**, 895 (1988).

[14] H. W. Sheng, K. Lu, and E. Ma, Acta Mater. **46**, 5195 (1998).

[15] Z. H. Jin, H. W. Sheng, and K. Lu, Phys. Rev. B **60**, 141 (1999).

[16] M. Schmidt, R. Kusche, W. Kronmüller, B. von Issendorf, and H. Haberland, Phys. Rev. Lett. **79**, 99 (1997).

[17] M. Schmidt, R. Kusche, B. von Issendorf, and H. Haberland, Nature (London) **393**, 238 (1998).

[18] S. L. Lai, J. Y. Guo, V. Petrova, G. Ramanath, and L. H. Allen, Phys. Rev. Lett. **77**, 99 (1996).

[19] S. L. Lai, G. Ramanath, L. H. Allen, P. Infante, and Z. Ma, Appl. Phys. Lett. **67**, 1229 (1995).

[20] S. L. Lai, G. Ramanath, and L. H. Allen, Appl. Phys. Lett. **70**, 43 (1997).

[21] S. L. Lai, J. R. A. Carlsson, and L. H. Allen, Appl. Phys. Lett. **72**, 1098 (1998).

[22] T. L. Tien-Yu, W. H. Lytle, and B. Hileman, IEEE Trans. Compon., Packag. Manuf. Technol., Part B **19**, 131 (1996).

[23] H.-P. Cheng and R. S. Berry, Phys. Rev. A **45**, 7969 (1992).

[24] R. Defay and I. Prigogine, *Surface Tension and Adsorption* (Wiley, New York, 1951) (English translation, 1966).

[25] P. Pawlow, Z. Phys. Chem. (Munich) **65**, 1 (1909); **65**, 545 (1909).

[26] H. Reiss and I. B. Wilson, J. Colloid Sci. **3**, 551 (1948).

[27] H. Sakai, Surf. Sci. **351**, 285 (1996).

[28] H. Reiss, P. Mirabel, and R. L. Whetten, J. Phys. Chem. **92**, 7241 (1988).

[29] P. R. Couchman and W. A. Jesser, Nature (London) **269**, 481 (1977).

[30] V. P. Skripov, V. P. Koverda, and V. N. Skokov, Phys. Status Solidi A **66**, 109 (1981).

[31] R. R. Vanfleet and J. M. Mochel, Surf. Sci. **341**, 40 (1995).

[32] A. Mori, M. Maruyama, and Y. Furukawa, J. Phys. Soc. Jpn. **65**, 2742 (1996).

[33] *CRC Handbook of Chemistry and Physics*, 78th ed. (CRC Press, Boca Raton, FL, 1997).

[34] F. S. Aires, P. Mélinon, M. Treilleux, G. Fuchs, A. Hoareau, and H. Roux, J. Phys. D **25**, 309 (1992); M. Treilleux, G. Fuchs, F. S. Aires, P. Mélinon, A. Hoareau, and B. Cabaud, Thin Solid Films **191**, 127 (1990).

[35] J. Knall, J.-E. Sundgren, G. V. Hansson, and J. E. Greene, Surf. Sci. **166**, 512 (1986).

[36] *Digital Image Processing Methods*, edited by E. R. Dougherty (Dekker, New York, 1994).

[37] A. M. Molenbroek, G. ter Horst, and J. W. M. Frenken, Surf. Sci. **365**, 103 (1996).

[38] *Handbook of the Physicochemical Properties of the Elements*, edited by G. V. Samsonov (IFI/Plenum, New York, 1968).

[39] D. R. Gaskel, in *Physical Metallurgy* (Elsevier, New York, 1983), Vol. 1, Chap. 6.